



Effect of partial oxidation and repolarization of TiC-derived nanoporous carbon electrodes on supercapacitor performance using a pH-neutral aqueous electrolyte

Maike Käärrik¹ · Mati Arulepp² · Jekaterina Kozlova³ · Jaan Aruväli⁴ · Uno Mäeorg¹ · Arvo Kikas³ · Vambola Kisand³ · Aile Tamm³ · Jaan Leis^{1,2}

Received: 4 March 2022 / Revised: 13 June 2022 / Accepted: 20 July 2022 / Published online: 1 August 2022
© The Author(s), under exclusive licence to Springer-Verlag GmbH Germany, part of Springer Nature 2022

Abstract

The present study considers TiC-derived carbon (CDC) and its partially oxidized derivative (ox-red-CDC) as potential electrode materials for pH-neutral aqueous electrolytes. The CDC was converted to ox-red-CDC by a modified Hummers' method involving back-reduction with hydrogen at 800 °C. Oxidation degraded the graphitic CDC structures, as shown by X-ray diffraction analysis, while scanning electron microscopy confirmed the exfoliation of graphene layers on the oxidized carbon surface. The changes in the surface chemistry of the carbon materials were studied by infrared, X-ray photoelectron, and energy-dispersive X-ray spectroscopy. The gas adsorption analysis showed a slight decrease in the volume of the subnanometer-sized pores during oxidation/reduction of CDC. To elucidate the relationships between the structure and electrochemical properties of carbon materials, cyclic voltammetry, galvanostatic cycling, and electrochemical impedance spectroscopy measurements were performed in 1 M Na₂SO₄ using 2- and 3-electrode test cells. The highest capacitance of 163 F g⁻¹ was demonstrated by pristine TiC-derived CDC in a symmetric 2-electrode cell. The asymmetric cell, which contained ox-red-CDC as an anode and pristine CDC as a cathode, had a slightly lower capacitance but an excellent cycling lifetime (specific capacitance increased by 7% after 5000 cycles). Temporary repolarization of 2-electrode cells during cycling improved both capacitance and power characteristics.

Keywords Nanoporous carbon · Carbide-derived carbon · Electrical double-layer capacitor · pH neutral electrolyte · Aqueous electrolyte

Introduction

Environmental issues related to energy management are becoming increasingly important, forcing humanity to pay more attention to the use of so-called green materials in energy storage technologies. Nanoporous carbon is one such green material, which, due to its large specific surface area

and favorable pore sizes, has proven to be an important electrode material for ultracapacitors, batteries, and fuel cells [1–3]. However, an electrical double-layer capacitor (EDLC) using a liquid electrolyte is the most attractive type of storage for nanoporous carbon electrodes, primarily because energy is stored in it by electroadsorption of the ions in nanopores. In the case of EDLCs, the principle is that the larger the carbon surface available to the electrolyte, the higher the capacitance of the device [4]. The effect of the pore size distribution (PSD) of carbon electrodes on capacitance has received much attention. It has been shown that the better the compatibility between the dimensions of the electrolyte ions and the carbon pores, the higher the capacitance [4–6]. Although the latter statement is quite well established for some organic electrolytes [5, 6], it has not been confirmed for aqueous electrolytes, where the effective size of ions for electroadsorption may differ significantly from that of bare ions due to strong ion solvates [3] and the redox processes

✉ Jaan Leis
jaan.leis@ut.ee

¹ Institute of Chemistry, University of Tartu, Ravila 14a, Tartu 50411, Estonia

² Skeleton Technologies, Valukoja 8, Tallinn 11415, Estonia

³ Institute of Physics, University of Tartu, W. Ostwald str. 1, Tartu 50411, Estonia

⁴ Institute of Ecology and Earth Sciences, University of Tartu, Vanemuise 46, Tartu 51014, Estonia

affect the value of the total capacitance mainly due to the narrow potential window (1.23 V, thermodynamically) of water [1].

Liquid electrolytes can be broadly divided into the following three classes: nonaqueous, aqueous, and ionic liquid electrolytes [7]. The requirements for electrolytes used in energy storage include chemical and electrochemical stability, a wide operating temperature range, high ion conductivity, low resistivity, and environmental friendliness [4, 7, 8]. In particular, due to the cost of organic electrolytes and environmental issues, there has been much emphasis recently on the study of aqueous electrolytes [9], especially electrolytes with a neutral pH, such as aqueous solutions of various alkali metal salts, such as sulfates and nitrates. The slightly lower capacitance obtained with pH-neutral electrolytes is compensated by their environmental friendliness and low cost [8]. It has also been shown that the use of neutral electrolytes makes it possible to operate over a wider voltage range (above 1.5 V) than alkaline and acidic electrolytes due to higher hydrogen overvoltage [10, 11]. Qu et al. studied the electrochemical performance of activated carbon at different scan rates in 0.5-M aqueous solutions of three alkali metal sulfates and showed that at higher scan rates, the capacitance increases with decreasing radius of hydrated ion ($\text{Li}^+ > \text{Na}^+ > \text{K}^+$) [12], thus suggesting that K^+ - and Na^+ -based aqueous electrolytes are better suited for supercapacitors than those using Li^+ cations. However, the better solubility of lithium salts compared to similar sodium or potassium salts is certainly a good reason why they have thus far received much more attention in various studies [10, 13–17]. Due to the strong solvation of Li^+ cations, it is also possible to achieve a wider operating voltage range. For example, using the Li_2SO_4 solution as an electrolyte, it reached 2.2 V without significant capacitive loss after 15,000 cycles [17].

In addition to matching the pore size of the electrode material to the ions of a particular electrolyte, other phenomena can be applied to increase the capacitance in aqueous electrolytes [4], for example, by incorporating pseudocapacitive components into the carbon matrix. Guo and Zheng showed that capacitance is related to both the high specific surface area of carbon and the presence of rich surface oxygen functional groups, providing pseudocapacitance in aqueous media [18]. Another study showed that the mild modification method of activated carbon with a persulfate solution is a valuable method to obtain electroactive oxygen functional groups on the carbon surface [19]. It was demonstrated that the increase in capacitance of the modified carbon using 1 M Na_2SO_4 electrolyte is proportional to the time of persulfate treatment. The ozonation process has also been used to enhance the functionalities of oxygen on the carbon surface, which increased both the specific capacitance and the efficiency of the electrochemical capacitors in aqueous media [20].

Nanoporous carbide-derived carbon (CDC) [21] with a well-tuned pore size distribution (PSD) has received much attention as a high-power electrode material [22–26]. The peculiarity of CDC is that the carbon particles retain the shape and dimensions of the original carbide and the textural and electronic properties of carbon depend on the chemical composition and structure of the parent carbide. This gives an opportunity to design carbon materials with the desired micro- and macrostructure by selecting a starting carbide and proper synthesis conditions [27]. In addition, the structure and surface functionality of CDC can be further tuned by chemical [28, 29] or physical activation [30–33].

Previous studies have also demonstrated that CDCs are suitable electrode materials for aqueous electrolytes, e.g., the specific capacitance of CDC at a low current density exceeds 200 F g^{-1} in 2 M H_2SO_4 [34]. Xu et al. found that the electrochemical performance of CDC depends on its hydrophilicity, and it was shown that the specific capacitance of graphitized TiC-derived CDC increases in an aqueous KOH electrolyte with varying amounts of ethanol from 5 F g^{-1} to 60 F g^{-1} at a scan rate of 20 mV s^{-1} [35, 36]. Eskusson et al. showed that Mo_2C -derived CDC with a hierarchical structure is a promising supercapacitor electrode material in a pH-neutral aqueous medium [37], demonstrating the high charge–discharge efficiency (98%) with 1 M Na_2SO_4 at $U \leq 1.0 \text{ V}$. The influences of ionic composition and concentration of pH-neutral aqueous electrolytes have been studied on directly electrospun TiC-derived CDC electrodes, which showed the highest gravimetric capacitances in 1 M NaNO_3 [38].

One of the issues with the use of nanoporous carbons in aqueous electrolytes is the hydrophobic surface of the carbon, which causes poor wettability. Another problem is the electrochemical stability of carbon, which is reduced by tangling bonds and structural defects acting as active centers for irreversible side reactions. Partial oxidation of the carbon has been found to counteract both problems. Gu et al. studied soaking TiC-derived CDC in a mixed acid solution containing HF and HNO_3 at room temperature, and as a result of acid treatment, the specific capacitance of the acid-soaked nano-TiC-CDC increased from 83 to 304 F g^{-1} at a scan rate of 5 mV s^{-1} in 6 M KOH aqueous electrolyte [39]. Gao et al. showed that deactivation of the carbon surface by chemical oxidation with H_2O_2 protects the positive carbon electrode from electro-oxidation during cell operation at higher voltages [10]. Recently, it was demonstrated that oxidation of CDC using the modified Hummers' method, originally developed as a fast and efficient method for the production of graphite oxide [40], improves the wettability of microporous carbon in aqueous electrolytes, and the capacitance of the resultant oxidized CDC was increased by 16 times in 6 M KOH [41]. This modified material also showed excellent cycling stability while retaining 92% of its capacitance

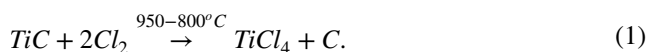
after 10,000 cycles. Hummers' oxidation method has also been used to modify a highly porous carbon aerogel, and the results proved the suitability of the modified carbon material for supercapacitors and batteries [42].

The major aim of this study is to provide new insights into carbon-based energy storage, for the first time considering nanoporous TiC-derived carbon with a moderately graphitized surface and its partially oxidized derivative as potential electrode materials for pH-neutral aqueous electrolytes. More specifically, 1 M Na₂SO₄ is used as the electrolyte to conduct the electrochemical characterization of CDC and its modified derivatives. Another aim of this study is to investigate the effect of Hummers' method, i.e., non-eroding oxidation, on the electrochemical performance of nanoporous carbon in a pH-neutral aqueous electrolyte and to determine the advantages and disadvantages of surface oxygen. Involving broad-based structural analysis of carbon materials, this work is thus the first comprehensive study of nanoporous and Hummers'-oxidized CDCs to elucidate the relationships between the structure and electrochemical performance of these materials in a pH-neutral aqueous electrolyte.

Experimental

Synthesis and modification of carbon materials

Nanoporous TiC-derived carbon (hereinafter referred to as CDC) with a partially graphitic surface was made by a gradual chlorination procedure of carbide at various temperatures [43]:



Titanium carbide powder (H.C. Starck, $\varnothing < 4 \mu\text{m}$, 75 g), placed in the horizontal tubular quartz reactor, was treated with chlorine gas (Linde Gas, 2.8, 1.5 l min⁻¹) for 15 min at 950 °C and then 180 min at 800 °C. The reactor was then purged with argon (Linde Gas, 4.0, 2 l min⁻¹) for 60 min at 1000 °C to remove residual chlorine and all gaseous by-products. Finally, the CDC powder was purified with hydrogen (Linde Gas, 4.0, 1 l min⁻¹) at 800 °C to dechlorinate and chemically reduce the carbon surface.

To oxidize CDC (ox-CDC), the CDC powder was chemically oxidized by Hummer's method [40], using NaNO₃ and KMnO₄ as the oxidizing agents and H₂SO₄ acid to improve the oxidation efficiency. Briefly, 1.0 g of CDC powder in 25 ml concentrated sulfuric acid was treated in an ultrasonic bath for 20 m, and then 1.0 g NaNO₃ and 3.0 g KMnO₄ were added at 0 °C. After that, the solution was stirred for 10 h at 35 °C and an additional 14 h at 20 °C. Then, 40 ml deionized water followed by 10 ml 30% H₂O₂ was added to the

oxidation solution. Finally, the oxidized CDC was filtered out and washed first with 10% HCl solution and then with distilled water.

To make the back-reduced CDC (ox-red-CDC), reduction of the dry ox-CDC powder was carried out in hydrogen (Linde Gas, 4.0, 1 l min⁻¹) flow for one hour at 800 °C.

Physicochemical characterization

The X-ray diffraction (XRD) spectra of the carbon powder samples were studied by a Bruker D8 Advance diffractometer. A scanning step of 0.020° (2 θ) from 3 to 93° (2 θ) and a total counting time of 522 s per step were used. The cell parameters were calculated using the full-profile analysis software Topas 6 (Bruker, Germany). Scanning electron microscopy (SEM) was chosen to visualize and study the surface morphology of carbon. The carbon material was attached to the SEM specimen stub using carbon conductive adhesive tape (TAAB Laboratories Equipment Ltd.). High-resolution SEM images at various magnifications were collected using a Helios NanoLab 600 (FEI) microscope. The elemental composition of carbon powder samples and the distribution of elements in these samples were performed in the same microscope by an energy dispersive X-ray spectrometer INCA Energy 350 (Oxford Instruments) equipped with an X-Max 50 mm² detector. The energy of the primary electrons used to acquire SEM images and determine the elemental composition was 10 keV. The EDX spectra and elemental maps were obtained and processed using INCA software (Oxford Instruments). The Fourier transform infrared (FT-IR) spectrum for carbon powder samples was recorded on a Bruker Alpha FTIR instrument using an ATR device with Ge crystal. X-ray photoelectron spectroscopy (XPS) studies of the surface functional groups of carbon samples, which contained 10 wt% PTFE compressed into a thin film with a size of 1 cm², were performed using a SCI-ENTA SES-100 electron spectrometer. For excitation, non-monochromatic Mg K α X-rays (photon energy 1253.6 eV) were used. Casa XPS software was used for the removal of the X-ray satellites, peak fitting (using the Gauss-Lorentz hybrid function and combination of linear and Shirley backgrounds) and calculation of concentrations.

Low-temperature nitrogen adsorption was measured at 77 K, and CO₂ adsorption was measured at 273 K using a NOVAtouch LX2 (Quantachrome Instruments) with TouchWin software (ver. 1.1). From the N₂ and CO₂ adsorption isotherms, PSD was calculated using a quenched solid density functional theory (QSDFT) and nonlocal density functional theory (NLDFT) models for slit-type pores, respectively. N₂ adsorption was also used to calculate total pore volume (V_{tot}) at a P/P_0 of 0.97 and specific surface area S_{BET} in the P/P_0 interval of 0.02–0.2 [44].

Electrochemical characterization

For electrochemical measurements, the carbon powder under study, including 10 wt% PTFE (Aldrich, 60% dispersion in water), was pressed into a film with a thickness of $100 \pm 10 \mu\text{m}$. The average densities of electrode discs cut out of the film were 0.71, 1.02, and 0.80 g cm^{-3} for CDC, ox-CDC, and ox-red-CDC, respectively. The carbon film for the counter electrode was made from activated carbon powder with $S_{\text{dft}} \sim 1600 \text{ m}^2 \text{ g}^{-1}$ (V2, EnerG2 Technologies Inc.) by using the same method described above. Prior to assembling the test cells for electrochemical testing, the carbon electrodes were treated under vacuum at $110 \text{ }^\circ\text{C}$ for 48 h.

Characterization of carbon materials was performed in 3-electrode test cells with gold current collectors and Ag|AgCl (3.5 M KCl) reference electrode (RE). The discs of the 7-mm diameter working electrode (WE) and a 16-mm diameter counter electrode (CE) were separated by a 1-mm-thick glass fiber separator (Whatman). A 1 M Na_2SO_4 (Fisher Chemical, anhydrous, 99.5%) in Milli-Q water as the electrolyte was used in all experiments. After assembly, the materials in the cell were allowed to soak in the electrolyte for approximately 24 h. The electrochemical measurements were performed using cyclic voltammetry (CV), galvanostatic, i.e., constant current (CC) methods, and electrochemical impedance spectroscopy (EIS). The potentiostat–galvanostat 1286 with FRA 1255B (Solartron) was used in all measurements. The anodic (0 to $+1.0 \text{ V vs. Ag|AgCl}$) and cathodic (0 to $-1.0 \text{ V vs. Ag|AgCl}$) performance of the materials was tested separately to avoid repolarization of the carbon material during the experiment. Prior to measurements, 3-electrode cells were preconditioned with 1000 CV cycles ($v = 20 \text{ mV s}^{-1}$) from 0 to $\pm 0.5 \text{ V vs. Ag|AgCl}$ according to the selected anode or cathode polarization to obtain reproducible test results.

The CV curves were measured at different potential scan rates, v , between 50 and 2 mV s^{-1} , starting from the highest scan rate. The CC measurements with positively and negatively charged electrodes were carried out with a current of 2 mA cm^{-2} ($\sim 0.3 \text{ A g}^{-1}$) from 0 to $\pm 0.75 \text{ V vs. Ag|AgCl}$. Before discharge, the test cell was kept at a constant potential ($\pm 0.75 \text{ V vs. Ag|AgCl}$) for 5 min to guarantee a full charge in all experiments (see discharge profile in Fig. S1). The specific capacitances of carbon materials (C_{CC} and C_{CV}) are given for the mass of carbon in the working electrode (Eqs. S1–S3). EIS measurements were performed in the frequency range of 1 MHz to 5 mHz at AC voltage of 5 mV using the ZView ver. 3.5i software (Scribner Associates Inc.). The series resistance, R_s , was determined by frequency response analysis and was calculated by equivalent circuit fitting using the series connection of R_s , C_s elements.

The cycling stability of carbon materials was evaluated in 2-electrode cells, which were assembled from two 7-mm

diameter electrodes attached to gold current collectors and separated with a 1-mm-thick Whatman separator. The cycling life was evaluated by using CV cycling at 20 mV s^{-1} in voltage intervals of 0–1.5 V. The specific capacitance of 2-electrode cells was expressed per weight of carbon in one electrode as $C = 4 \times (C_{\text{cell}}/m_C)$, where m_C is the total weight of the active carbon in the cell. The changes in resistance were measured by EIS.

Results and discussion

Structure and textural properties of carbon materials

The CDC sample was prepared from TiC by gradual chlorination at various temperatures, starting at $950 \text{ }^\circ\text{C}$ and ending with the conversion of TiC to CDC at $800 \text{ }^\circ\text{C}$, which resulted in nanoporous carbon with a hierarchical pore size distribution [43]. The method is based on the fact that the structural order of CDC is controlled by the synthesis temperature [22, 45, 46]. The higher temperature ($950 \text{ }^\circ\text{C}$ in this study) applied at the beginning of chlorination results in more graphitic surface layers of the CDC particles, which in turn should increase the electrical conductivity between the particles when such carbon is used as the electrode material. To investigate the behavior of partially oxidized surfaces on the electrochemical properties of nanoporous carbon, a sample of TiC-derived CDC was oxidized by Hummers' method to ox-CDC and then reduced back to ox-red-CDC with hydrogen at $800 \text{ }^\circ\text{C}$.

SEM images (Fig. 1) show that the oxidizing process does not influence the macroscopic structure of carbon particles. The oxidized particles retain their original shape without a notable change in particle size (Fig. 1a, d, g). However, on high-resolution images (Fig. 1c, f, i), clear signs of oxidation are visible on the surface of ox-CDC and ox-red-CDC compared to pristine CDC. Because the nanoporous CDC used in this study contained a slightly graphitic surface, oxidation formed wavy graphene layers on the surface, which is a typical picture of the exfoliation of graphite due to Hummers' oxidation [40, 47, 48].

Degradation of the graphitic structure by oxidation is also evidenced by XRD spectra. Figure 2a shows the diffraction patterns of the CDC, ox-CDC, and ox-red-CDC materials. In all spectra, the broad (10) diffraction peak at $\sim 43^\circ$ (2θ) can be seen, reflecting the in-plane order of hexagonal carbon as typical of disordered nanoporous carbon [23, 49]. The sharp (002) diffraction peak at $\sim 26^\circ$ (2θ) observed in the pattern of pristine CDC disappeared from ox-CDC and ox-red-CDC. This phenomenon is consistent with SEM observations and reveals that the graphite domains in the pristine CDC material are damaged during oxidation. It is also worth noting that

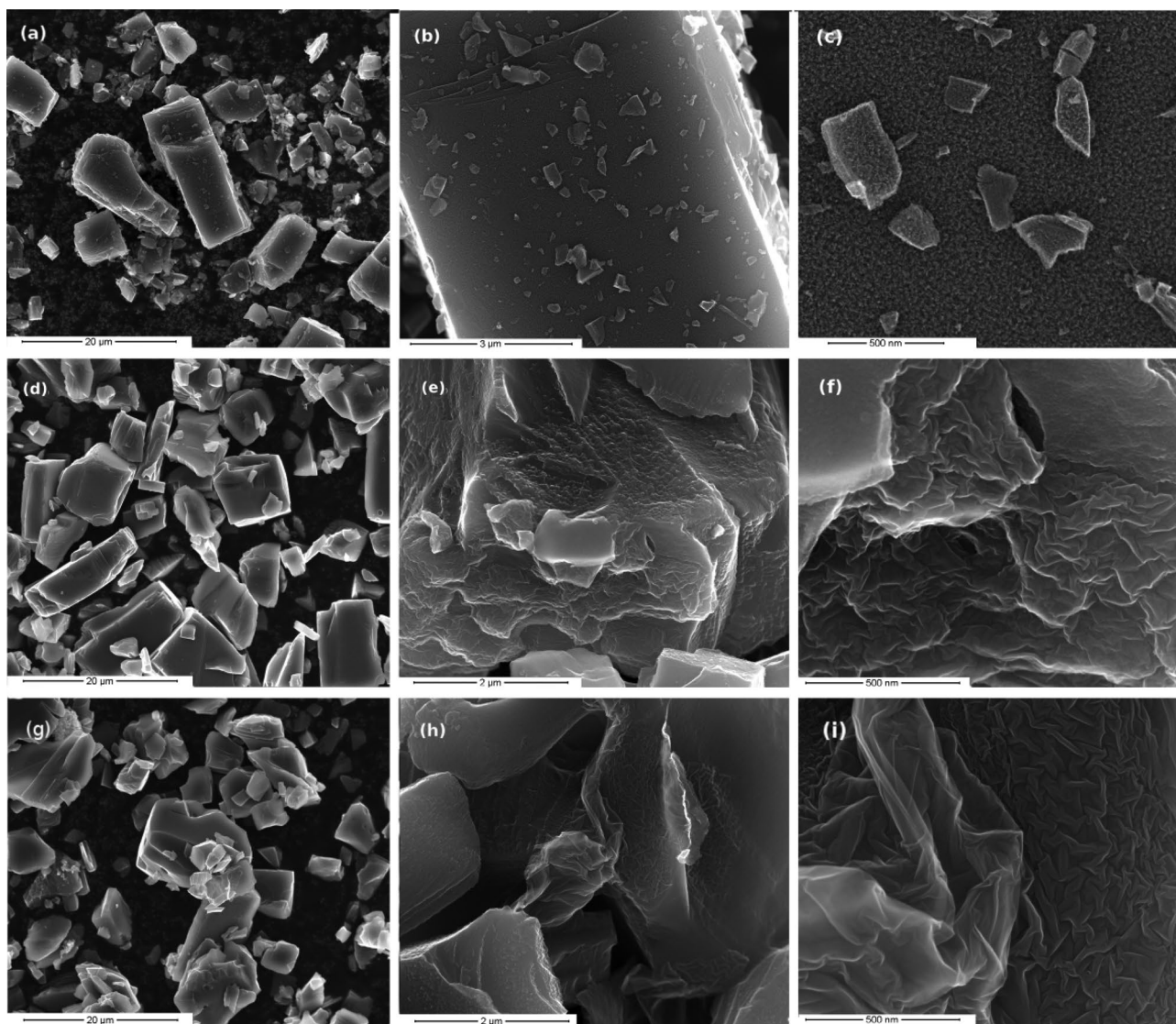


Fig. 1 SEM images of different magnifications of CDC (a, b, c), ox-CDC (d, e, f), and ox-red-CDC (g, h, i)

the graphitic structure is not recovered after the reduction of ox-CDC, while the tendency of graphene layers to reassembly back into graphite is a known issue with the reduction of graphene oxide to graphene [50].

The textural properties of CDC and its oxidized derivatives were studied using physisorption of nitrogen and carbon dioxide. The N_2 adsorption–desorption isotherms of all three materials studied (Fig. 2b) are typical type Ia isotherms according to the IUPAC classification [51], which is characteristic of microporous materials. Analysis of the textural data (Table 1) shows that the oxidizing process significantly reduces the specific surface area and volume of micropores of ox-CDC compared to pristine CDC. The decrease in porosity parameters is assumed to be partly because of the increased mass of a sample by the oxygen-containing groups and partly due to the blocking of the carbon surface by these

groups. Back-reduction of ox-CDC is expected to remove most of the oxygen groups, and correspondingly, the specific surface area S_{BET} increases from 879 to 1300 $\text{m}^2 \text{g}^{-1}$ but remains lower than the value of pristine CDC before oxidation, which was almost 1500 $\text{m}^2 \text{g}^{-1}$.

Oxidation/reduction treatments do not alter the PSD profile, i.e., locations of pore size maxima of carbon materials (*cf.* Fig. 2c). Based on N_2 adsorption, all three materials are almost completely microporous, with a narrow pore size distribution at approximately 0.8 nm and a small shoulder at approximately 1.5 nm (see Fig. 2c). However, the difference can be seen in the volumes of fractions with different pore sizes. While oxidation decreases the volume of pores of all sizes relative to the pristine CDC, upon reduction of ox-CDC, both the larger micropores (1–2 nm) and mesopores (2–50 nm) of the ox-red-CDC restore the same volume as

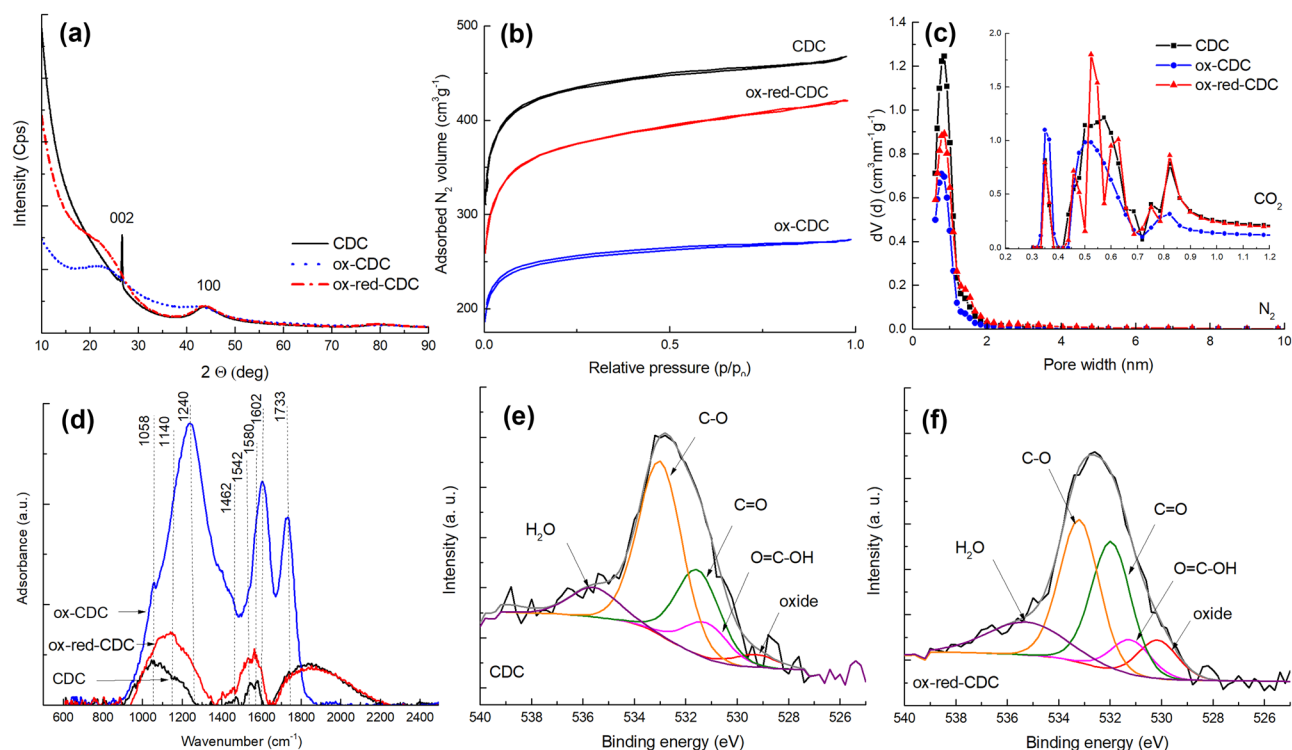


Fig. 2 XRD patterns (a), N₂ adsorption–desorption isotherms (b), pore size distributions calculated from N₂ and CO₂ isotherms (c), and IR spectra of carbon samples (d), and XPS core-level spectra in the O1s region of CDC (e), and ox-red-CDC (f) materials

in the pristine CDC, but the volume of small micropores (< 1 nm) remains notably below that of CDC, i.e., 0.38 vs. 0.49 cm³ g⁻¹, respectively (see Table 1).

According to the EDX analysis, the oxygen contents of the CDC, ox-CDC, and ox-red-CDC powders are 3.4 ± 0.9, 23.1 ± 2.0, and 5.2 ± 0.6 wt%, respectively, and oxygen is rather evenly distributed within all three samples (see Fig. S2). The changes in the oxygen-containing groups on the carbon surface due to oxidation/reduction treatment were detected by FT-IR analysis (see Fig. 2d). Comparing the spectra of the pristine CDC and ox-red-CDC, there is no significant difference between the types of oxygen groups, but clearly, the oxygen content of the surface of the reduced material is higher. The vibrations at approximately 1000–1200 cm⁻¹ in both the CDC and ox-red-CDC spectra belong to different oxygen-containing functional groups,

such as carboxyl or epoxy groups, but due to the overlap of adsorption, the exact identification of the groups is complicated [52, 53]. The weak peak at 1460 cm⁻¹ can be attributed to CH₃ or CH₂ bending vibrations [52]. The broad signal observed at 1540–1580 cm⁻¹ usually belongs to C=C vibrations in aromatic rings; however, it has also been assigned to the C=O stretching vibration of carbonyl groups [52–54]. The broad peak with the maximum at 1850 cm⁻¹ is difficult to interpret unambiguously; however, it has been associated with C=O stretching in anhydrides or lactones [55, 56]. The vibration spectrum of ox-CDC is significantly different from those of the other two materials. It shows distinguishable intense peaks at approximately 1240 and 1730 cm⁻¹, which are caused by C-O and C=O stretching in different oxygenated surface groups, respectively. There is also a clear peak at approximately 1600 cm⁻¹, which would normally be

Table 1 Specific surface areas (S_{BET} and S_{dft}), total pore volumes (V_t), and volumes of different pore size fractions ($V_{<x \text{ nm}}$) calculated from N₂ isotherms and $V_{<0.7 \text{ nm}}$ calculated from CO₂ adsorption

Carbon Sample	S_{BET} (m ² g ⁻¹)	S_{dft} (m ² g ⁻¹)	V_t (cm ³ g ⁻¹)	$V_{<2 \text{ nm}}$ (cm ³ g ⁻¹)	$V_{<1 \text{ nm}}$ (cm ³ g ⁻¹)	$V_{<0.7 \text{ nm}}$ (cm ³ g ⁻¹)
CDC	1499	1511	0.73	0.63	0.49	0.24
ox-CDC	879	934	0.42	0.37	0.30	0.21
ox-red-CDC	1300	1285	0.65	0.54	0.38	0.22

associated with C=C stretching in the aromatic ring. In ox-CDC, however, the peak is most likely caused by vibrations of the carbonyl groups that are directly conjugated with the polyaromatic matrix [53, 56, 57].

The surface oxygen of CDC and ox-red-CDC carbon films containing 10% PTFE binder was also analyzed by XPS (survey spectra in Fig. S3), which showed total surface oxygen contents of 1.0 and 1.9 at%, respectively. The high-resolution analysis of the O1s region (see Figs. 2e, f, and S4a) confirmed the IR finding that the proportion of all oxygen-containing groups is higher for the ox-red-CDC material, with the number of C=O carbonyl groups having increased the most, from 0.24 to 0.59 at% (cf. Fig. S4b).

Electrochemical study

The cycling voltammetry (CV) study of nanoporous CDC materials was performed in 1-M aqueous Na_2SO_4 using a 3-electrode test cell with an Ag|AgCl reference electrode. Figure 3 shows the CV curves of CDC and ox-red-CDC at various potential windows up to an interval of -0.9 to 0.9 V, which characterizes the capacitive behavior of these materials. In the case of ox-red-CDC, polarization toward positive potential values causes oxidation of the carbon at $E \sim 0.4$ V and reduction of surface functional groups at close to 0 V vs. Ag|AgCl. It is pertinent to mention that analogous redox peaks are absent in the CV curves of both pristine CDC and ox-CDC, i.e., starting material of ox-red-CDC (see Fig. S5).

In view of the fact that repolarization of electrodes is not allowed in conventional supercapacitors, such as EDL capacitors, the CDC and ox-red-CDC materials with cathodic or anodic polarization potential were studied in more detail using 3-electrode cells. To avoid repolarization

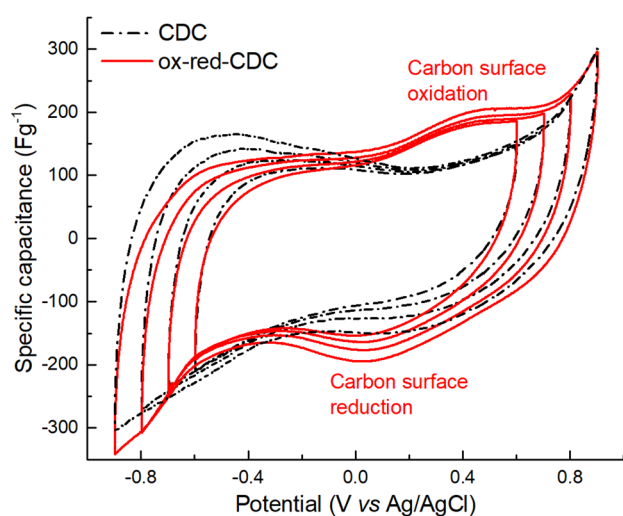


Fig. 3 CV plots of carbon materials expressed as C vs. potential measured at a voltage scan rate of 5 mV s^{-1}

of the electrodes under study, separate cells were used for positive and negative polarization. The capacitance of the materials at opposite polarization potentials was studied by CC method (2 mA cm^{-2} ; $0 \text{ V to } +/ -0.75 \text{ V}$). Capacitance values (see Tables 2 and S1) were measured after one thousand preconditioning charge–discharge cycles performed at 20 mV s^{-1} in a potential range of $0 \text{ V to } +0.5 \text{ V}$ or $0 \text{ V to } -0.5 \text{ V}$, depending on whether the positively or negatively polarized electrode was tested. Due to the hydrophobic surface of the electrodes and the hindered access to the micropores, a long preconditioning was required. The CDC was rather stable during preconditioning; the C_{cc}^- improved from 124 to 134 F g^{-1} , while the C_{cc}^- of ox-red-CDC improved almost threefold, from 42 to 120 F g^{-1} (see Table S1).

The data in Table 2 show that the oxidation/reduction treatment decreased the capacitance of pristine CDC by 10–20%. The main reason for the lower capacitance of ox-red-CDC is more likely to be the blocking of submicron pores by surface functional groups added during the oxidation/reduction treatment of CDC. As previously shown, the capacitance of nanoporous CDC materials is related to the size of pores accommodating the electrolyte ions [5]. The difference between the capacitance of CDC and ox-red-CDC can thus partly be explained by the compatibility between the pore sizes of these carbons and the sizes of the electrolyte ions used (the diameters of hydrated Na^+ and SO_4^{2-} are 0.72 and 0.76 nm, respectively) [58, 59]. The textural properties in Table 1 show that the ox-red-CDC has approximately 25% smaller volume of $< 1\text{-nm}$ pores compared to the pristine CDC, while the mesoporous volume is the same for both materials. This difference in the volume of small micropores is in good agreement with the approximately 20% difference in capacitance of both materials. Another factor that may slightly reduce the gravimetric capacitance is the higher oxygen content of ox-red-CDC, which adds weight to the carbon material. Some discrepancies between CC and CV capacitances (see Table S1) are due to the differences in methodologies, in particular the 5-min hold of potential before CC discharging.

The CV curves of the negatively polarized CDC material (Fig. 4a) do not contain red-ox peaks over a wide potential range (0 to -1.0 V), reflecting the typical behavior of EDL materials with good charge propagation. The capacitance of the nanoporous CDC depends significantly on the

Table 2 Specific capacitance of CDC and ox-red-CDC by constant current cycling at negative and positive potentials

Carbon sample	$C_{cc}^- (\text{F g}^{-1})$	$C_{cc}^+ (\text{F g}^{-1})$
CDC	134	126
ox-red-CDC	120	104

potential—the wider the potential window is, the higher the capacitance obtained. In the case of the positive polarization of the CDC, no significant evidence of redox processes up to approximately 0.8 V is observed. However, by further increasing the potential window, the curves acquire an asymmetric shape, and a characteristic carbon oxidation peak appears at $E > 0.8$ V. Reduction of the oxidized functional groups is reflected by the peak at 0.3–0.4 V (see Fig. 4a).

Ox-red-CDC behaves similarly to CDC at negative potentials up to -0.8 V (Fig. 4b) and, as with CDC, its CV curves show the potential dependence of capacitance on cathodic polarization. At a wider potential window, however, a weak hydrogen adsorption peak occurs at approximately -0.75 V (vs. Ag/AgCl), which amplifies as the potential window is expanded to -1.0 V. In the case of anodic polarization, ox-red-CDC is electrochemically more stable than CDC; electrochemical oxidation/reduction of the carbon surface appears only when 0.9 V is reached during cycling. Better resistance to oxidation of the carbon surface may be due to the passivated, partly oxygen-functionalized carbon surface in the ox-red-CDC.

To compare the electrochemical stability of CDC and ox-red-CDC, two symmetric cells, CDC/CDC and ox-red-CDC/ox-red-CDC, and one unsymmetrical ox-red-CDC/CDC cell (anode/cathode, respectively) were composed (see definitions in Table S2). Prior to testing, the 2-electrode cells were preconditioned by 120 CV cycles (0 – 1.5 V, 20 mV s^{-1}). Capacitance of the cells was then measured at different scan rates: 50 , 20 , 10 , 5 , 2 mV s^{-1} (see Fig. S6). The specific capacitance values at the beginning of the cycling life test, after 5000 cycles, and after repolarization 20 mV s^{-1} and 2 mV s^{-1} are shown in Fig. 7.

The highest specific capacitance of 163 F g^{-1} per carbon was measured for the CDC cell by applying CC at 2 mA cm^{-2} (Fig. 5a). Significantly lower capacitance was obtained for the ox-red-CDC cell with an initial capacitance of 98 F g^{-1} per carbon. The unsymmetrical cell resulted in 135 F g^{-1} per carbon, which is close to the mean value of the capacitances of anode and cathode materials measured in 3-electrode cells.

Charging–discharging of the 2-electrode cells up to 5000 cycles was performed using CV at a voltage scan rate of 20 mV s^{-1} in the voltage range of 0 to 1.5 V. Good electrochemical stability was observed for all three cells. The changes in capacitance and resistance during cycling are presented in Fig. 5b, c. Usually, we expect the capacitance of the cell to decrease over time due to undesired electrochemical side processes on the carbon surface and/or the physical degradation of the electrodes due to thermal effects and expansion contractions during charging–discharging. Indeed, this can be observed with the CDC cell, which shows a small decrease in capacitance during 5000 charge–discharge cycles. A slight decrease in capacitance is also observed for the ox-red-CDC cell during the first 2000 cycles, but then it starts to increase until reaching approximately 105% of the initial value. The unsymmetrical cell behaves differently; during approximately 4000 cycles, its capacitance constantly increases, reaching 108% of the initial capacitance within the mentioned period. In general, both the ox-red-CDC and the unsymmetrical cells reached the maximum capacitance by approximately 4000 cycles (see Fig. 5b).

The values of cell resistance were determined from the series resistance R_s at 0.5 V and 1 kHz. A CDC cell shows typical behavior with a characteristic increase in R_s with an increase in the number of cycles (Fig. 5c). However, both

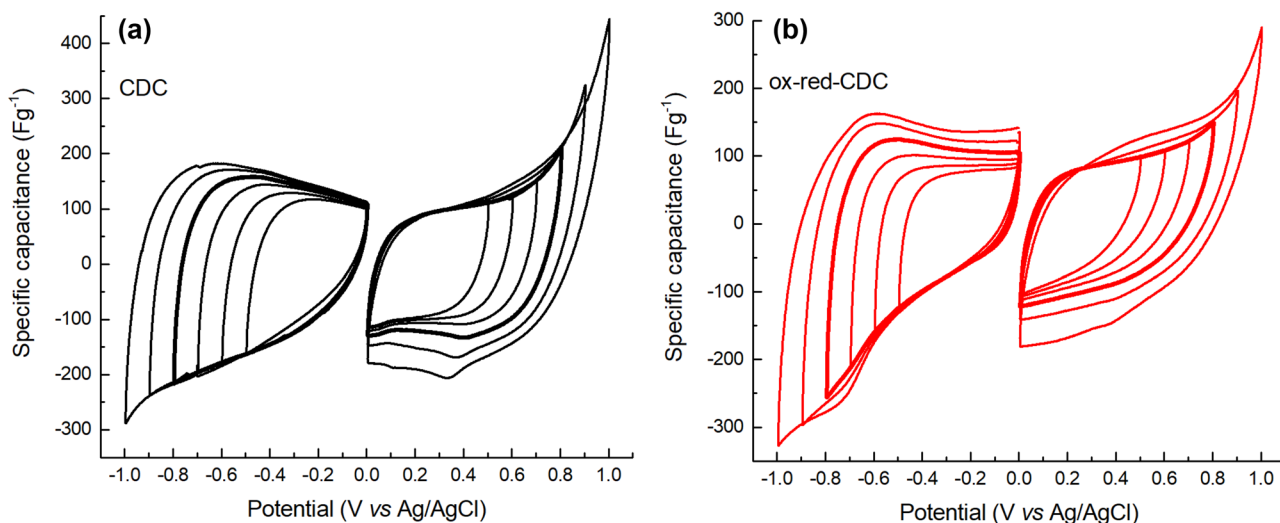


Fig. 4 Cyclic voltammograms ($v=2$ mV s^{-1}) for positively and negatively charged electrodes of CDC (a) and ox-red-CDC (b). The cycles in bold were used to calculate the C_{CV} capacitance

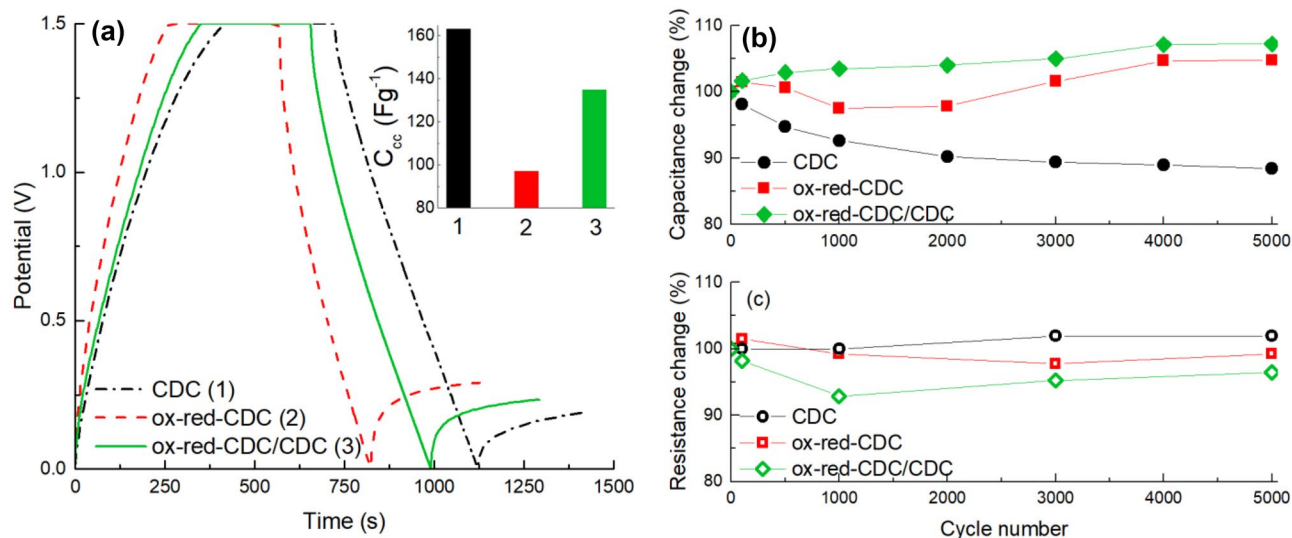


Fig. 5 CC charge–discharge curves ($I=2 \text{ mA cm}^{-2}$) and respective discharge capacitance (in inset) measured for 2-electrode cells before cycling life test (a) and retention in capacitance (b) and resistance (c),

the ox-red-CDC and unsymmetrical cells show a decrease in R_s during the first 1000–2000 cycles, after which the R_s increases somewhat and stabilizes at approximately the initial resistance value. This unusual behavior of unsymmetrical and ox-red-CDC cells is likely due to the slow conditioning of the ox-red-CDC electrode, as seen in the 3-electrode experiments.

Comparing the R_s vs. frequency dependences, the CDC cell showed very stable results (Fig. 6a). However, the ox-red-CDC and unsymmetrical cells revealed a decrease in resistance during cycling, wherein a significant decrease (approximately 20% during 5000 cycles) takes place at lower frequencies, at $f < 0.1 \text{ Hz}$ (see Fig. 6b, c). In the Nyquist plot (Fig. 6d), the CDC cell shows a typical response of microporous electrode, with very low changes in the cycling life test. The slope of nearly 45° at lower Z' values is the so-called porous region, which is characteristic to the mass-transfer limited processes in micro- and mesopores. The Nyquist plot gradually approaches a more vertical slope at higher Z' values ($> 50 \Omega$), which corresponds to so-called EDLC region. Similar behavior is observed during cycling of the unsymmetrical cell (Fig. 6f), where the Nyquist curve gradually acquires the shape of a classical porous electrode curve, with an initial slope of 45° and forming a consistently more vertical line at $Z' \sim 100 \Omega$. This indicates a significant decrease in the impedance in the micropores and an improvement in the capacitance due to the improved adsorption–desorption equilibrium on the electrolyte/carbon interface during the cycling life test. The Nyquist graph (see the insets in Fig. 6d–f) shows at very high frequencies that the starting point of the curves ($Z''=0$) is constant in all test cells, confirming that the resistance at the gold collector/carbon electrode interface does not

determined for the 2-electrode cells using CV (at 20 mV s^{-1}) and EIS methodologies, respectively

alter during cycling and that the cells resist corrosion very well. All cells show a barely perceptible semicircle at high frequencies that progresses slightly during cycling, which may be due to an increasing charge transfer resistance (or some rapid chemical reaction) at the carbon/electrolyte interface.

To evaluate the effect of repolarization on 2-electrode cells, the polarities of the current terminals of all three cells were reversed after 5000 cycles, followed by 10 CV cycles between 0 and 1.5 V. Thereafter, the initial polarities were re-established, and the cells were then charged–discharged for another 1000 cycles by using a voltage scan rate of $v=20 \text{ mV s}^{-1}$. The specific capacitances of all three cells per carbon at 20 mV s^{-1} and 2 mV s^{-1} are shown in Fig. 7. The overall result is that after repolarization, all cells tested acquire a significantly higher capacitance than immediately before repolarization. An increase in capacitance was observed with both 20 and 2 mV s^{-1} scan rates. For example, in the case of an unsymmetrical cell, after passing 5000 cycles with repolarization followed, the specific capacitance per carbon material increased from 75 to 92 F g^{-1} and from 116 to 137 F g^{-1} at 20 and 2 mV s^{-1} (Fig. 7c), respectively. Over the next 1000 cycles after repolarization treatment, both the CDC cell and unsymmetrical cell behave similarly and lose capacitance, restoring approximately the same capacitance as before repolarization. Again, ox-red-CDC behaves differently, and its capacitance continues to increase during postrepolarization cycling. Similar phenomena have been described in recent articles, where repolarization of a cell has been found to prolong its lifespan [60] and increase its capacitance [13].

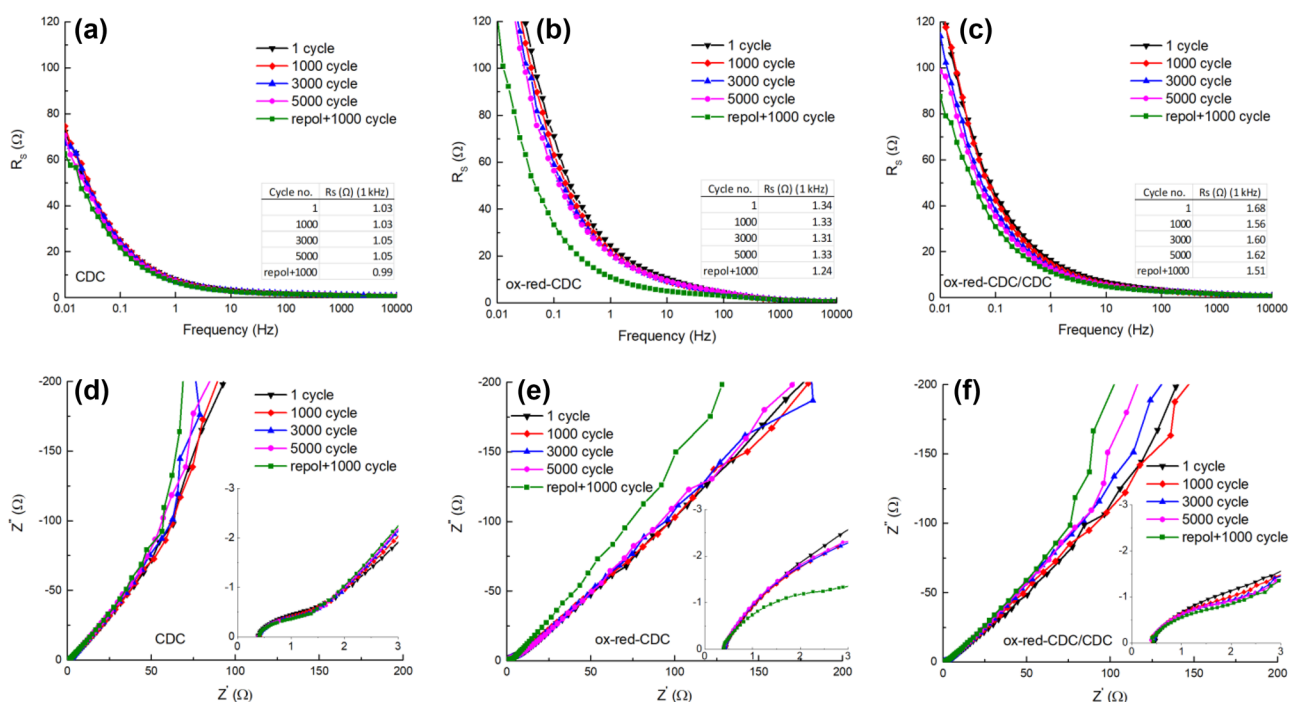


Fig. 6 The dependences of R_s vs. frequency of the CDC (a), ox-red-CDC (b), unsymmetrical cells (e), and Nyquist plots of CDC (d), ox-red-CDC (e), and unsymmetrical cells (f) at 0.5 V, measured during

the cycling life test including a short-term repolarization after the 5000th cycle. Insets in Nyquist plots show a low-impedance region

The main reason for the increase in capacitance after temporary short-term repolarization is probably the “cleaning” of the surface of the carbon electrode from the adsorbed or deposited surface blocking compounds due to a unidirectional potential. Repolarization brings electrostatically or otherwise weakly bound surface compounds back into solution, freeing the surface for electrosorption of electrolyte ions. It is also possible that some of the electroactive groups bound to the carbon surface are reduced or oxidized during this process, depending on the potential. Additionally, the population of ions at the

interface immediately after repolarization may be larger until a new equilibrium is reached. Better filling of very small micropores (perhaps with possible release of gas molecules generated during cycling) due to the more intense movement of ions initiated by the change in polarization may also play a role. An important observation is that immediately after temporary repolarization, there is a significant decrease in the resistance (R_s) of ox-red-CDC and unsymmetrical cells (see Fig. 6b, c). However, the mechanism of the decrease in resistance is not completely the same: while in the case of ox-red-CDC, the decrease

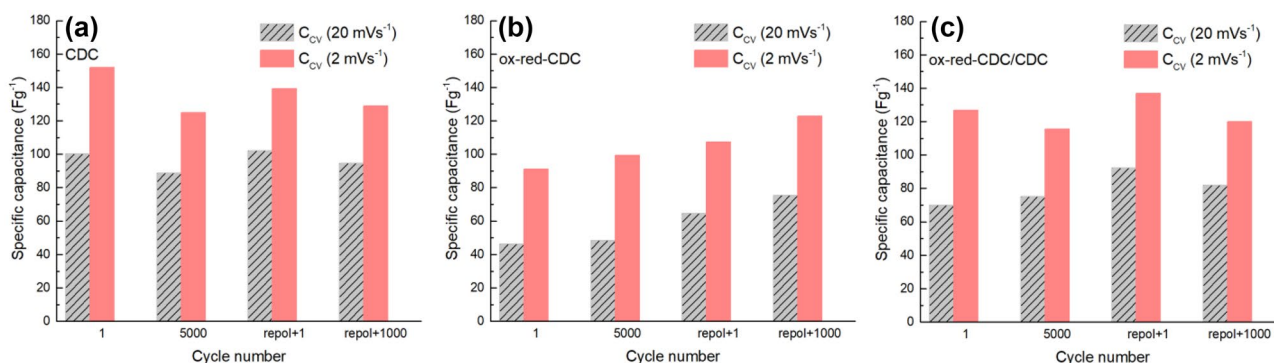


Fig. 7 The specific capacitance of 2-electrode cells at the beginning of the cycling life test, after 5000 cycles, immediately after repolarization and after 1000 cycles

in resistance occurs over a very wide frequency range (see Fig. 6b), in the asymmetrical cell, a change in R_s is observed only at low frequencies (see Fig. 6c). In the case of ox-red-CDC, the decrease in R_s is likely to be due to a decrease in impedance from the carbon surface groups, which is accompanied by a new charge transfer process (small arc formation in Fig. 6e), suggesting an additional reaction at the carbon/electrolyte interface. In the case of a hybrid cell, R_s decreases due to a decrease in impedance at the carbon/electrolyte interface in micro- and mesopores, i.e., due to partial purification of the porous surface upon repolarization.

To understand how much repolarization affects the capacitance of CDC and ox-red-CDC electrodes at both positive and negative polarization, these electrodes were tested on repolarization separately in 3-electrode cells. It was found that after repolarization, both the cathodic and anodic capacitances of ox-red-CDC increased significantly; C_{cc}^- improved from 120 to 154 F g⁻¹, and C_{cc}^+ improved from 104 to 160 F g⁻¹. The CDC electrode has a smaller increase in capacitance, especially for anodic capacitance: the C_{cc}^- from 134 to 163 F g⁻¹ and the C_{cc}^+ from 126 to 140 F g⁻¹. Therefore, it can be assumed that the repolarization of ox-red-CDC used as the anode material is mainly responsible for an increase in the capacitance of the entire hybrid cell after repolarization (Fig. 7).

The dependence of energy vs. power, i.e., the so-called Ragone plot, constructed from the data of CV measurements (cf. Fig. 8) expresses the energy storage behavior of an unsymmetrical cell over the cycling life test, including the repolarization effect. The Ragone plot shows that the

energy density of the cell is rather stable over cycling in the low power region (the highest value of 18 Wh kg⁻¹ per carbon at 91 W kg⁻¹), while the power performance significantly improves during cycling due to decreasing resistance. Over 5000 charge–discharge cycles, the specific energy per carbon increases from 7 Wh kg⁻¹ to 11 Wh kg⁻¹ at $P=421$ W kg⁻¹. Further improvement is observed after temporary repolarization, after which the next 1000 cycles increase the specific energy per carbon up to 12 Wh kg⁻¹ at $P=421$ W kg⁻¹. Based on these results, we can claim that CDC and its partially oxidized derivative are promising electrode materials for energy storage in pH-neutral aqueous electrolytes.

Conclusion

In this research, nanoporous TiC-derived carbon with a moderately graphitized surface and its partially oxidized derivative, ox-red-CDC, were synthesized and thoroughly characterized as conceivable materials for energy storage, particularly for electrochemical double-layer capacitors using a pH-neutral aqueous electrolyte. It was shown that Hummers' oxidation method, followed by back-reduction with hydrogen, largely preserves the specific surface area of the nanoporous material. However, a small decrease in S_{BET} of ox-red-CDC from 1500 to 1300 m² g⁻¹ was observed compared to the pristine CDC due to a decrease in porosity in the submicron pore diameter range, as shown by N₂ and CO₂ physisorption analysis. SEM analysis confirmed that, at the macroscopic level, ox-red-CDC retains the structure of pristine CDC, whereas the high-resolution SEM images show corrugated graphene layers formed on ox-red-CDC because of the oxidation of the partly graphitic CDC surface. Decomposition of the graphitic CDC structure due to oxidation was also detected by XRD. The oxidation/reduction treatment increased the overall oxygen content of CDC 1.5-fold, as revealed by SEM–EDX. This observation was in good agreement with the results of FT-IR and XPS analysis, which confirmed a higher proportion of all oxygen-containing groups in the ox-red-CDC, with the largest increase in C=O groups compared to the pristine CDC.

Electrochemical characterization of nanoporous CDC and its partially oxidized derivative, ox-red-CDC, was performed in a 1 M Na₂SO₄ electrolyte. The highest capacitance of ~160 F g⁻¹ (per carbon) was measured for pristine TiC-derived CDC, which was also an expected result due to its higher volume of subnanometer pores compared to ox-red-CDC. Ox-red-CDC has a lower capacitance of 135 F g⁻¹ but much better resistance to oxidation at positive potentials up to ~1 V vs. Ag|AgCl, which indicates that Hummers' oxidation successfully passivates active centers on the surface of nanoporous CDC. Therefore, the partially

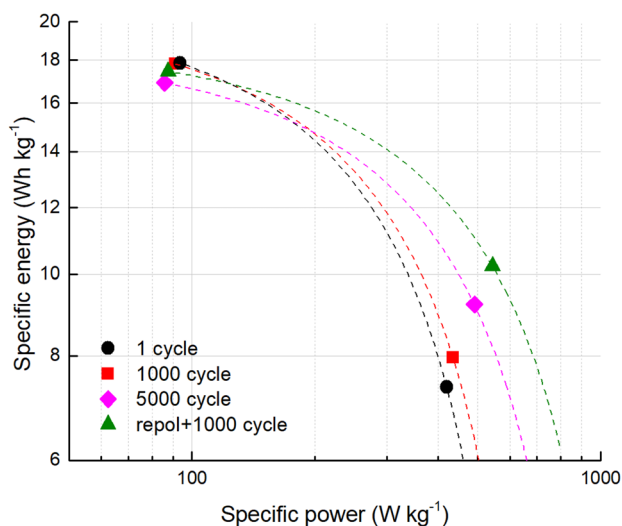


Fig. 8 Specific energy vs. specific power of the unsymmetrical cell during the cycling life test including temporary repolarization after the 5000th cycle

oxidized ox-red-CDC would be useful as an anode material for unsymmetric carbon/carbon ultracapacitor. Outstanding electrochemical stability was achieved in an unsymmetric 2-electrode cell containing ox-red-CDC as an anode and pristine CDC as a cathode. It was unusual for this cell to continuously improve its properties in terms of both resistance and capacitance over 5000 charge–discharge cycles, which may be due to the slow electrochemical formation of the ox-red-CDC anode. The latter phenomenon can be caused by oxygen-containing functional groups on the carbon surface, which interact with electrolyte ions and limit their electrosorption on carbon.

Very intriguing results were obtained when studying the effect of repolarization on 2-electrode cells in a cycling life study. After a temporary repolarization, all cells tested acquired significantly higher capacitance than immediately before repolarization; the largest increase of 10% was demonstrated by a symmetric cell comprising both electrodes from ox-red-CDC. However, considering both the capacitance and the electrochemical stability, the unsymmetrical cell with the ox-red-CDC anode and pristine CDC cathode gave the best output. This cell retains the capacitance during the 5000th cycle, and the increase in capacitance after repolarization is also quite considerable—from 115 to 137 F g^{-1} (measured by CV at a scan rate of 2 mV s^{-1}).

The results presented show the high potential of nanoporous partly oxidized CDC, especially as the anode material, to be used in pH-neutral aqueous electrolytes. Temporary repolarization has also been shown to be a useful strategy that can significantly extend the life of pH-neutral aqueous electrolyte-based capacitors containing oxidized porous carbon electrodes.

Supplementary Information The online version contains supplementary material available at <https://doi.org/10.1007/s10008-022-05253-4>.

Acknowledgements This work was financially supported by the Ministry of Education and Research, Republic of Estonia, through the Estonian Research Council [grant number PRG1509] and the European Union through the European Regional Development Fund [grant numbers TK143 “Center of Excellence in Molecular Cell Engineering” and TK134 “Emerging Orders in Quantum and Nanomaterials”].

References

- Béguin F, Frackowiak E (2013) Supercapacitors: materials, systems, and applications. Wiley-VCH, Weinheim
- Conway BE (1999) Electrochemical supercapacitors: scientific fundamentals and technological applications. Springer Science+Business Media, New York
- Inagaki M, Konno H, Tanaïke O (2010) Carbon materials for electrochemical capacitors. *J Power Sources* 195:7880–7903. <https://doi.org/10.1016/j.jpowsour.2010.06.036>
- Béguin F, Presser V, Balducci A, Frackowiak E (2014) Carbons and electrolytes for advanced supercapacitors. *Adv Mater* 26:2219–2251. <https://doi.org/10.1002/adma.201304137>
- Käärik M, Arulepp M, Käärik M et al (2020) Characterization and prediction of double-layer capacitance of nanoporous carbon materials using the quantitative nano-structure-property relationship approach based on experimentally determined porosity descriptors. *Carbon* 158:494–504. <https://doi.org/10.1016/j.carbon.2019.11.017>
- Käärik M, Maran U, Arulepp M et al (2018) Quantitative nano-structure–property relationships for the nanoporous carbon: predicting the performance of energy storage materials. *ACS Appl Energy Mater* 1:4016–4024. <https://doi.org/10.1021/acsaeam.8b00708>
- Mirzaeiian M, Abbas Q, Ogbu A et al (2017) Electrode and electrolyte materials for electrochemical capacitors. *Int J Hydrog Energy* 42:25565–25587. <https://doi.org/10.1016/j.ijhydene.2017.04.241>
- Frackowiak E, Abbas Q, Béguin F (2013) Carbon/carbon supercapacitors *J Energy Chem* 22:226–240. [https://doi.org/10.1016/S2095-4956\(13\)60028-5](https://doi.org/10.1016/S2095-4956(13)60028-5)
- Zhong C, Deng Y, Hu W et al (2015) A review of electrolyte materials and compositions for electrochemical supercapacitors. *Chem Soc Rev* 44:7484–7539. <https://doi.org/10.1039/C5CS00303B>
- Gao Q, Demarconnay L, Raymundo-Piñero E, Béguin F (2012) Exploring the large voltage range of carbon/carbon supercapacitors in aqueous lithium sulfate electrolyte. *Energy Environ Sci* 5:9611. <https://doi.org/10.1039/c2ee22284a>
- Demarconnay L, Raymundo-Piñero E, Béguin F (2010) A symmetric carbon/carbon supercapacitor operating at 1.6V by using a neutral aqueous solution. *Electrochem Commun* 12:1275–1278. <https://doi.org/10.1016/j.elecom.2010.06.036>
- Qu QT, Wang B, Yang LC et al (2008) Study on electrochemical performance of activated carbon in aqueous Li_2SO_4 , Na_2SO_4 and K_2SO_4 electrolytes. *Electrochem Commun* 10:1652–1655. <https://doi.org/10.1016/j.elecom.2008.08.020>
- Fic K, He M, Berg EJ et al (2017) Comparative operando study of degradation mechanisms in carbon-based electrochemical capacitors with Li_2SO_4 and LiNO_3 electrolytes. *Carbon* 120:281–293. <https://doi.org/10.1016/j.carbon.2017.05.061>
- He M, Fic K, Frackowiak E et al (2016) Ageing phenomena in high-voltage aqueous supercapacitors investigated by in situ gas analysis. *Energy Environ Sci* 9:623–633. <https://doi.org/10.1039/C5EE02875B>
- Piwek J, Platek A, Frackowiak E, Fic K (2019) Mechanisms of the performance fading of carbon-based electrochemical capacitors operating in a LiNO_3 electrolyte. *J Power Sources* 438:227029. <https://doi.org/10.1016/j.jpowsour.2019.227029>
- Fic K, Platek A, Piwek J et al (2019) Revisited insights into charge storage mechanisms in electrochemical capacitors with Li_2SO_4 -based electrolyte. *Energy Storage Mater* 22:1–14. <https://doi.org/10.1016/j.ensm.2019.08.005>
- Fic K, Lota G, Meller M, Frackowiak E (2012) Novel insight into neutral medium as electrolyte for high-voltage supercapacitors. *Energy Environ Sci* 5:5842–5850. <https://doi.org/10.1039/C1EE02262H>
- Guo J, Zheng P (2018) Improving the capacitance of derived porous carbon by oxygen functional groups for supercapacitor. *Mater Lett* 214:134–137. <https://doi.org/10.1016/j.matlet.2017.11.083>
- Kopczyński K, Pęziak-Kowalska D, Lota K et al (2017) Persulfate treatment as a method of modifying carbon electrode material for aqueous electrochemical capacitors. *J Solid State Electrochem* 21:1079–1088. <https://doi.org/10.1007/s10008-016-3452-8>
- Lota G, Krawczyk P, Lota K et al (2016) The application of activated carbon modified by ozone treatment for energy storage. *J Solid State Electrochem* 20:2857–2864. <https://doi.org/10.1007/s10008-016-3293-5>
- Presser V, Heon M, Gogotsi Y (2011) Carbide-derived carbons - from porous networks to nanotubes and graphene. *Adv Funct Mater* 21:810–833. <https://doi.org/10.1002/adfm.201002094>

22. Leis J, Arulepp M, Käärik M, Perkson A (2010) The effect of Mo₂C derived carbon pore size on the electrical double-layer characteristics in propylene carbonate-based electrolyte. *Carbon* 48:4001–4008. <https://doi.org/10.1016/j.carbon.2010.07.003>
23. Leis J, Arulepp M, Kuura A et al (2006) Electrical double-layer characteristics of novel carbide-derived carbon materials. *Carbon* 44:2122–2129. <https://doi.org/10.1016/j.carbon.2006.04.022>
24. Arulepp M, Leis J, Lätt M et al (2006) The advanced carbide-derived carbon based supercapacitor. *J Power Sources* 162:1460–1466. <https://doi.org/10.1016/j.jpowsour.2006.08.014>
25. Chmiola J, Yushin G, Dash R, Gogotsi Y (2006) Effect of pore size and surface area of carbide derived carbons on specific capacitance. *J Power Sources* 158:765–772. <https://doi.org/10.1016/j.jpowsour.2005.09.008>
26. Dash R, Chmiola J, Yushin G et al (2006) Titanium carbide derived nanoporous carbon for energy-related applications. *Carbon* 44:2489–2497. <https://doi.org/10.1016/j.carbon.2006.04.035>
27. Gogotsi Y, Nikitin A, Ye H et al (2003) Nanoporous carbide-derived carbon with tunable pore size. *Nat Mater* 2:591–594. <https://doi.org/10.1038/nmat957>
28. Portet C, Lillo-Ródenas MÁ, Linares-Solano A, Gogotsi Y (2009) Capacitance of KOH activated carbide-derived carbons. *Phys Chem Chem Phys* 11:4943. <https://doi.org/10.1039/b816514a>
29. Kierzek K, Frackowiak E, Lota G et al (2004) Electrochemical capacitors based on highly porous carbons prepared by KOH activation. *Electrochim Acta* 49:515–523. <https://doi.org/10.1016/j.electacta.2003.08.026>
30. Osswald S, Portet C, Gogotsi Y et al (2009) Porosity control in nanoporous carbide-derived carbon by oxidation in air and carbon dioxide. *J Solid State Chem* 182:1733–1741. <https://doi.org/10.1016/j.jssc.2009.04.017>
31. Käärik M, Arulepp M, Kook M et al (2017) Characterisation of steam-treated nanoporous carbide-derived carbon of TiC origin: structure and enhanced electrochemical performance. *J Porous Mater*. <https://doi.org/10.1007/s10934-017-0517-8>
32. Kormann M, Popovska N (2010) Processing of carbide-derived carbons with enhanced porosity by activation with carbon dioxide. *Microporous Mesoporous Mater* 130:167–173. <https://doi.org/10.1016/j.micromeso.2009.10.028>
33. Tee E, Tallo I, Lust E et al (2019) Electrical double layer capacitors based on steam and CO₂-steam co-activated carbon electrodes and ionic liquid electrolyte. *J Electrochem Soc* 166:A1558–A1567. <https://doi.org/10.1149/2.0811908jes>
34. Fernández JA, Arulepp M, Leis J et al (2008) EDLC performance of carbide-derived carbons in aprotic and acidic electrolytes. *Electrochim Acta* 53:7111–7116. <https://doi.org/10.1016/j.electacta.2008.05.028>
35. Xu J, Zhang R, Chen P, Ge S (2014) Effects of adding ethanol to KOH electrolyte on electrochemical performance of titanium carbide-derived carbon. *J Power Sources* 246:132–140. <https://doi.org/10.1016/j.jpowsour.2013.07.069>
36. Xu J, Zhang R, Wu C et al (2014) Electrochemical performance of graphitized carbide-derived-carbon with hierarchical micro- and meso-pores in alkaline electrolyte. *Carbon* 74:226–236. <https://doi.org/10.1016/j.carbon.2014.03.026>
37. Eskusson J, Jänes A, Kikas A et al (2011) Physical and electrochemical characteristics of supercapacitors based on carbide derived carbon electrodes in aqueous electrolytes. *J Power Sources* 196:4109–4116. <https://doi.org/10.1016/j.jpowsour.2010.10.100>
38. Malmberg S, Arulepp M, Laanemets K, et al (2021) The performance of fibrous cdc electrodes in aqueous and non-aqueous electrolytes. *C* 7:46. <https://doi.org/10.3390/c7020046>
39. Gu Y, Liu K, Zhang X, Zhang R (2019) Huge enhancement in electrochemical performance of nano carbide-derived carbon obtained by simply room-temperature soaking treatment in HF and HNO₃ mixed solution. *J Porous Mater* 26:1241–1248. <https://doi.org/10.1007/s10934-019-00724-y>
40. Hummers WS, Offeman RE (1958) Preparation of graphitic oxide. *J Am Chem Soc* 80:1339–1339. <https://doi.org/10.1021/ja01539a017>
41. Zhang X, Yan P, Zhang R, Xue X (2017) A strategy for constructing the compact carbon structure with high volumetric performance for supercapacitors from porous carbons. *Int J Hydrog Energy* 42:6166–6172. <https://doi.org/10.1016/j.ijhydene.2016.11.171>
42. Xu Y, Ren B, Wang S et al (2018) Carbon aerogel-based supercapacitors modified by hummers oxidation method. *J Colloid Interface Sci* 527:25–31. <https://doi.org/10.1016/j.jcis.2018.04.108>
43. Leis, J, Arulepp M, Lätt, M, Kuura, H (2010) A method of making the porous carbon material and porous carbon materials produced by the method. US7, 803, 345
44. Brunauer S, Emmett PH, Teller E (1938) Adsorption of gases in multimolecular layers. *J Am Chem Soc* 60:309–319. <https://doi.org/10.1021/ja01269a023>
45. Lätt M, Käärik M, Permann L et al (2010) A structural influence on the electrical double-layer characteristics of Al₄C₃-derived carbon. *J Solid State Electrochem* 14:543–548. <https://doi.org/10.1007/s10008-008-0659-3>
46. Käärik M, Arulepp M, Karelson M, Leis J (2008) The effect of graphitization catalyst on the structure and porosity of SiC derived carbons. *Carbon* 46:1579–1587. <https://doi.org/10.1016/j.carbon.2008.07.003>
47. Santamaría-Juárez G, Gómez-Barojas E, Quiroga-González E et al (2020) Safer modified Hummers' method for the synthesis of graphene oxide with high quality and high yield. *Mater Res Express* 6:125631. <https://doi.org/10.1088/2053-1591/ab4cbf>
48. Muzyka R, Kwoka M, Smędowski Ł et al (2017) Oxidation of graphite by different modified Hummers methods. *New Carbon Mater* 32:15–20. [https://doi.org/10.1016/S1872-5805\(17\)60102-1](https://doi.org/10.1016/S1872-5805(17)60102-1)
49. Peikola A-L, Uibu M, Kozlova J et al (2021) Carbon xerogel from 5-methylresorcinol-formaldehyde gel: The controllability of structural properties. *Carbon Trends* 3:100037. <https://doi.org/10.1016/j.cartre.2021.100037>
50. Chen Y, Zhang Z, Huang Z, Zhang H (2017) Effects of oxygen-containing functional groups on the supercapacitor performance of incompletely reduced graphene oxides. *Int J Hydrog Energy* 42:7186–7194. <https://doi.org/10.1016/j.ijhydene.2016.08.054>
51. Thommes M, Kaneko K, Neimark AV et al (2015) Physisorption of gases, with special reference to the evaluation of surface area and pore size distribution (IUPAC Technical Report). *Pure Appl Chem*. <https://doi.org/10.1515/pac-2014-1117>
52. Teng L, Tang T (2008) IR study on surface chemical properties of catalytic grown carbon nanotubes and nanofibers. *J Zhejiang Univ-Sci A* 9:720–726. <https://doi.org/10.1631/jzus.A071503>
53. Țucureanu V, Matei A, Avram AM (2016) FTIR spectroscopy for carbon family study. *Crit Rev Anal Chem* 46:502–520. <https://doi.org/10.1080/10408347.2016.1157013>
54. Yang L, Huang T, Jiang X, Jiang W (2016) Effect of steam and CO₂ activation on characteristics and desulfurization performance of pyrolysis modified activated carbon. *Adsorption* 22:1099–1107. <https://doi.org/10.1007/s10450-016-9832-7>
55. Kohl S, Drochner A, Vogel H (2010) Quantification of oxygen surface groups on carbon materials via diffuse reflectance FT-IR spectroscopy and temperature programmed desorption. *Catal Today* 150:67–70. <https://doi.org/10.1016/j.cattod.2009.05.016>
56. Zhuang Q-L, Kiyotani T, Tomita A (1994) DRIFT and TK/TPD Analyses of surface oxygen complexes formed during carbon gasification. *Energy Fuels* 8:714–718. <https://doi.org/10.1021/ef00045a028>
57. Silva AMT, Machado BF, Figueiredo JL, Faria JL (2009) Controlling the surface chemistry of carbon xerogels using HNO₃-hydrothermal oxidation. *Carbon* 47:1670–1679. <https://doi.org/10.1016/j.carbon.2009.02.022>
58. Li Y, Zhang C, Jiang Y et al (2016) Effects of the hydration ratio on the electrosorption selectivity of ions during capacitive deionization. *Desalination* 399:171–177. <https://doi.org/10.1016/j.desal.2016.09.011>

59. Nightingale ER (1959) Phenomenological theory of ion solvation. Effective Radii of Hydrated Ions. *J Phys Chem* 63:1381–1387. <https://doi.org/10.1021/j150579a011>
60. Piwek J, Platek-Mielczarek A, Frackowiak E, Fic K (2021) Enhancing capacitor lifetime by alternate constant polarization. *J Power Sources* 506:230131. <https://doi.org/10.1016/j.jpowsour.2021.230131>

Publisher's Note Springer Nature remains neutral with regard to jurisdictional claims in published maps and institutional affiliations.

Springer Nature or its licensor holds exclusive rights to this article under a publishing agreement with the author(s) or other rightsholder(s); author self-archiving of the accepted manuscript version of this article is solely governed by the terms of such publishing agreement and applicable law.